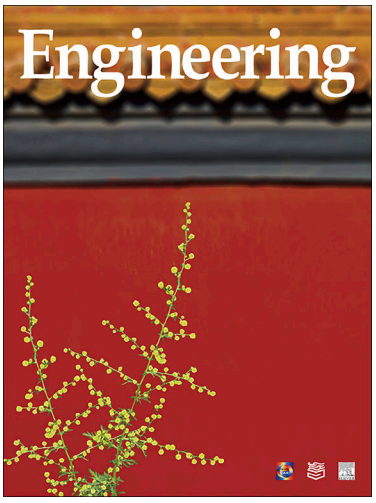
Journal Pre-proofs



Article

Terrain-Aware Autonomy for Self-Reconfigurable Rovers Informed by Zhurong *In Situ* Datasets from Utopia Planitia

Liang Ding, Huanan Qi, Tianyi Yu, Ximing He, Haibo Gao, Miao Zheng, Xinyu Li, Chuankai Liu, Baofeng Yuan, Xinyan Guo, Wenhao Feng, Lisijin Tang, Xiaohui Liu, Zuoyu Zhang, Ruyi Zhou, Huaiguang Yang, Jing Sun, Houman Yu, Sen Liu, Yafang Liu, Yuncheng Lin, Shaojin Han, Qian Xu, Lichun Li, Hao Lu, Ping Jiang, Pierangelo Masarati, Zdravko Terze, Zongquan Deng

PII: S2095-8099(26)00577-1
DOI: https://doi.org/10.1016/j.eng.2026.08.031
Reference: ENG 2491

To appear in: *Engineering*

Received Date: 22 January 2026
Revised Date: 13 July 2026
Accepted Date: 7 August 2026

Please cite this article as: L. Ding, H. Qi, T. Yu, X. He, H. Gao, M. Zheng, X. Li, C. Liu, B. Yuan, X. Guo, W. Feng, L. Tang, X. Liu, Z. Zhang, R. Zhou, H. Yang, J. Sun, H. Yu, S. Liu, Y. Liu, Y. Lin, S. Han, Q. Xu, L. Li, H. Lu, P. Jiang, P. Masarati, Z. Terze, Z. Deng, Terrain-Aware Autonomy for Self-Reconfigurable Rovers Informed by Zhurong *In Situ* Datasets from Utopia Planitia, *Engineering* (2026), doi: https://doi.org/10.1016/j.eng.2026.08.031

This is a PDF of an article that has undergone enhancements after acceptance, such as the addition of a cover page and metadata, and formatting for readability. This version will undergo additional copyediting, typesetting and review before it is published in its final form. As such, this version is no longer the Accepted Manuscript, but it is not yet the definitive Version of Record; we are providing this early version to give early visibility of the article. Please note that Elsevier's sharing policy for the Published Journal Article applies to this version, see: https://www.elsevier.com/about/policies-and-standards/sharing#4-published-journal-article. Please also note that, during the production process, errors may be discovered which could affect the content, and all legal disclaimers that apply to the journal pertain.

© 2026 THE AUTHORS. Published by Elsevier LTD on behalf of Chinese Academy of Engineering and Higher Education Press Limited Company

Journal Pre-proofs

Journal Pre-proofs

Research

Mechanical Engineering—Article

Terrain-Aware Autonomy for Self-Reconfigurable Rovers Informed by Zhurong *In Situ* Datasets from Utopia Planitia

Liang Ding [a,#], Huanan Qi [a,d,#], Tianyi Yu [b,#], Ximing He [b], Haibo Gao [a,*], Miao Zheng [a], Xinyu Li [a], Chuankai Liu [b], Baofeng Yuan [c], Xinyan Guo [a], Wenhao Feng [a], Lisijin Tang [a], Xiaohui Liu [b], Zuoyu Zhang [b], Ruyi Zhou [a], Huaiguang Yang [a], Jing Sun [c], Houman Yu [c], Sen Liu [a], Yafang Liu [c], Yuncheng Lin [c], Shaojin Han [b], Qian Xu [b], Lichun Li [b], Hao Lu [b], Ping Jiang [b], Pierangelo Masarati [d], Zdravko Terze [e], Zongquan Deng [a]

[a] *State Key Laboratory of Robotics and Systems, Harbin Institute of Technology, Harbin 150001, China*

[b] *Beijing Aerospace Control Center, Beijing 100094, China*

[c] *China Academy of Space Technology, Beijing 100044, China*

[d] *Department of Aerospace Science and Technology, Politecnico di Milano, Milan 20156, Italy*

[e] *Faculty of Mechanical Engineering and Naval Architecture, University of Zagreb, Zagreb 10000, Croatia*

* Corresponding author.

E-mail address: gaohaibo@hit.edu.cn (H. Gao).

[#]These authors contributed equally to this work.

Journal Pre-proofs

Abstract: Terrain-aware autonomy is critical for rovers to safely traverse heterogeneous surfaces. Multimode mobility across loose sand and sharp relief remains challenging because mode switching, which induces mechanical reconfiguration, is constrained by reduced contact stability. This study developed a terrain-aware autonomy control framework incorporating multimode mobility, informed by *in situ* datasets from China's Zhurong Mars rover in Utopia Planitia, and subsequently validated it using an Earth-based

prototype. *In situ* traverse logs and imagery spanning 359 sols were analyzed to quantify the wheel–terrain interaction and wheel-rolling mobility limits. Autonomous obstacle-avoidance drives achieved longer traverses per drive than Earth-commanded drives (mean 13.9 m vs 6.1 m), and slip-sinkage statistics were used to update Martian sinkage parameters. Obstacle morphologies extracted from close-range images were further systematically categorized into terrain undulations, surface obstacles, and topographic barriers by linking terrain characteristics to traverse-interruption conditions. A mechanics-constrained action library of 120 maneuvers was constructed and grouped into six basic mobility modes, including body creeping and wheel lifting. A "Look, Touch, and Move" strategy is proposed for multimode decision-making through fuzzy logic safety gating. Efficient waypoint cruising was experimentally demonstrated on a Mars-analog test site using a Zhurong Mars rover prototype, where five representative obstacle types were overcome with online replanning and nine autonomous mode switches.

Keywords: Mars exploration; Planetary rover; Autonomous cruise; Multimode mobility; Terramechanics

1. Introduction

An approximately 22 min communication delay and limited onboard computation impose fundamental constraints on continuous ground intervention and autonomous planning for Mars planetary rovers [1]. To extend traverse range and maximize scientific outcomes, terrain-aware autonomy has been increasingly recognized as a key control objective [2]. As exploration targets shift toward scientifically interesting regions with stronger relief, heterogeneous regolith, and abundant hazards, rover mobility is limited by the mismatch between a single wheel-rolling mode and diverse terrain-traversal challenges [3]. Accordingly, multimode autonomy control for self-reconfigurable rovers should advance beyond geometric hazard avoidance towards integrated perception–decision–execution methods, where terrain–obstacle characteristics are parameterized and mapped to admissible and safe motion actions.

Landed planetary rovers have been developed with varying levels of autonomy. In early Mars rovers, such as Spirit and Opportunity, operations were primarily based on ground-generated commands, while safeguarded driving, AutoNav, and later visual-odometry-based slip compensation were progressively introduced to improve mobility performance [4–6]. For Curiosity, higher-rate onboard state estimation and terrain-adaptive mobility risk mitigation were further integrated [7,8]. In Perseverance, autonomy was further advanced through improved onboard perception and navigation, upgraded path planning, and higher-level decision support, enabling longer autonomous traverses in complex terrain [9,10]. Accordingly, traverse challenges have frequently been associated with wheel–terrain interaction conditions on Mars [11]. Loose bedforms and steep slopes are associated with increased wheel slip and sinkage, and rocky fields and sharp relief are associated with wheel overloading, chassis obstruction, and forced replanning [3]. Significant advances have been reported in learning- or perception-assisted traversability evaluation and terrain-aware path planning [12,13], as well as in terrain-adaptive control strategies [8]. However, the systematic integration of terrain morphology into different modes of mobility execution remains limited. Motion hazards are primarily handled through geometric avoidance and conservative safety termination under a wheel-rolling assumption [14,15]. Lunar rover operations have mainly been conducted through crewed driving or low-latency supervised teleoperation, with waypoint planning and hazard assessment strongly dependent on ground-based vision products [16,17]. By contrast, this study targeted the multimode decision (MD)–obstacle traversal (OT) (MD–OT) layer for self-reconfigurable rovers: the executable action space is expanded through

a mechanics-constrained action library, and a terrain-contact-aware mode gate is implemented to map the obstacle morphology to admissible mobility modes. Moreover, the algorithmic computational load and attainable onboard intelligence remain key design considerations for planetary mobile systems, motivating lightweight decision schemes, such as fuzzy logic algorithms [18,19].

Rover vision-based localization, including visual inertial odometry (VIO), is used for map fusion and decision-making but remains uncertain owing to traversal length drift, feature degeneracy, and imagery-motion timing misalignment [20,21]; these uncertainties are increased by blur and rapid viewpoint changes during reconfiguration motion. Obstacle maps from stereo elevation mapping are also uncertain owing to disparity noise, range-dependent degradation, and discretization from grid resolution [22,23]. These input uncertainties can be incorporated into uncertainty-aware mapping and iterative belief-space replanning under probabilistic safety constraints [24]. To reduce VIO-related localization uncertainty, camera attitude stabilization is implemented through an online coordinate frame reset routine to maintain viewing-geometry consistency during rover traversal, consistent with [25]. In planetary rover localization, vision-based pose estimates can be complemented by wheel-based measurements through multi-sensor fusion, often within a Kalman filter-based state estimation framework [26]. In this study, a VIO-based localization method was used as a controlled baseline for evaluating terrain-aware multimode mobility, rather than as a spaceflight-qualified multi-sensor navigation architecture.

To connect perceived terrain morphology with multimode locomotion feasibility without relying on high-fidelity rover–environment interaction models, this study introduces a general methodology. The Zhurong Mars rover was employed as an *in situ* reference platform, and the developed autonomy control framework was validated through Earth-based experiments using a Zhurong-like rover prototype. The main novelty is a contact state-aware mapping from terrain morphology to mode admissibility, in which obstacle geometry is converted into mode feasibility constraints and online safety margins using a compact set of low-complexity intelligent algorithms. Specifically, terrain contact conditions are represented by a unified contact surface complexity descriptor synthesized from roughness- and steepness-related parameters, enabling consistent characterization across heterogeneous obstacle types without imposing a single hard slope/roughness cutoff. This descriptor is further coupled with motion-state descriptors that capture wheel load redistribution and trajectory-tracking smoothness, thereby providing comparable safety margins across distinct mechanical configurations. The rover multimode autonomy control problem is then formulated as a terrain morphology-driven decision process with lightweight onboard computation while remaining constrained by mechanism reconfiguration.

In this study, a terrain-aware autonomy control framework was developed for self-reconfigurable rovers, informed by the Zhurong *in situ* dataset. Trajectory planning (TP) is defined as the first module, within which VIO provides vision-inertial localization for terrain reconstruction and state estimation. An optimal mobility mode is then determined by the MD module, and the selected motion actions are executed by the OT module. Specifically, the slip and sinkage statistics of the Zhurong Mars rover are used to update Martian soil sinkage parameters through a wheel–soil interaction model. The conditions that interrupt wheel-rolling autonomous cruise are summarized by analyzing the rover steering curvature and obstacle size from synchronized drive logs and imagery. Terrain traversal challenges are then organized by systematically classifying the observed obstacle geometry and morphology into three categories: terrain undulations (TUs), surface obstacles (SOs), and topographic barriers. A multimode action library for Zhurong-like self-reconfigurable rovers is

constructed by jointly imposing constraints on the spatial coordination of movable joints and on the timing and sequencing of action execution. Considering the rover's mechanism limits, the library comprises 120 discrete actions, including wheel lifting, chassis lifting, creeping, and wheel crabbing. The action library constructed in the OT module is integrated into the autonomy framework in a closed loop by the proposed three-layer "Look, Touch, and Move" decision strategy implemented in the MD module, in which perceived obstacle characteristics are mapped to an optimal mobility mode. Additionally, fuzzy logic gating indices are defined to link the characterized obstacle and contact conditions to the safe selection of motion modes and their deployment. The feasibility of the developed control framework was validated at a Mars-analog test site using a Zhurong-like rover prototype across five representative obstacle types, demonstrating reliable autonomous cruise enabled by multimode mobility.

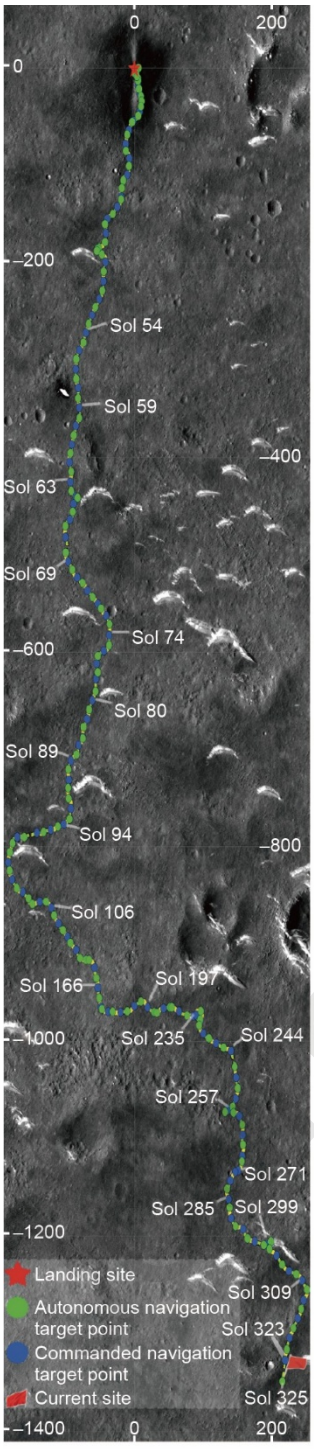
2. Methods

2.1. Wheeled locomotion performance of the Zhurong Mars rover and traversal challenges

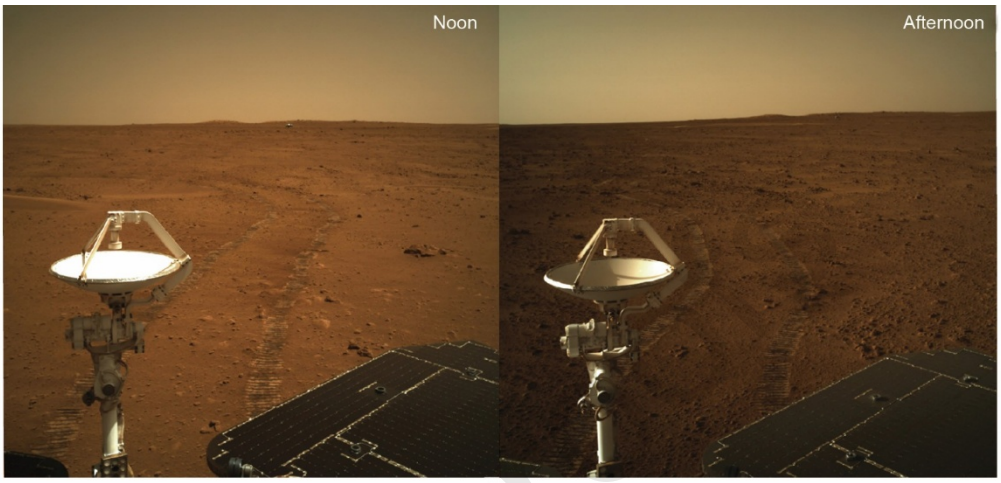
The Zhurong Mars rover landed in southern Utopia Planitia on 15 May 2021, within a low-elevation, generally smooth sector of the northern lowlands that was selected for both engineering safety and scientific interest [27]. The landing area is characterized by diverse geomorphic features, including impact craters, pitted cones, troughs, mesas/ridges, and widespread aeolian bedforms, such as dunes and transverse aeolian ridges [28]. Orbital and *in situ* observations further indicate a dusty, fine-grained surface with relatively low rock abundance and locally variable roughness [29]. The site is also close to geomorphic contacts that have been associated with possible shoreline formation and other marine or water-related processes [30,31].

Over 359 Martian days, the rover drove a total of 1921.5 m in wheel-rolling mode, executed in two cruise submodes: 110 Earth-commanded drives (EMD) covering 673.3 m and 90 autonomous obstacle-avoidance drives (AOAD) covering 1248.2 m (Fig. 1(a) and Table 1). Compared with EMD, AOAD increased the mean distance traveled per commanded drive from 6.1 to 13.9 m during flat-terrain traverse evaluations, corresponding to an approximately 127% improvement in cruise efficiency. This analysis excluded nontraverse motions, including approach and positioning maneuvers, in-place turns without net translation, and other short drives constrained by operational requirements.

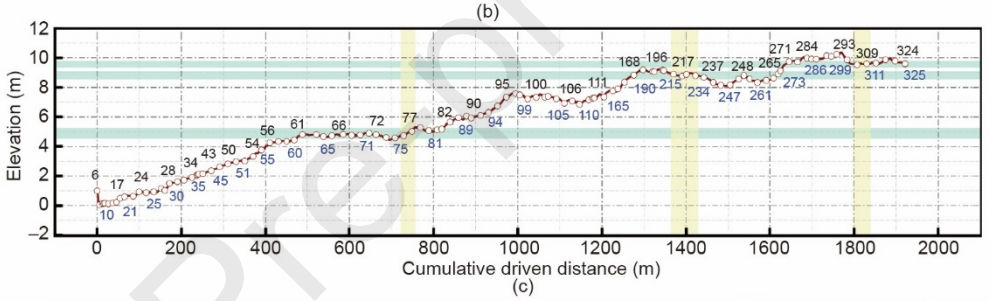
Journal Pre-proofs


0
200
0
−200
Sol 54
Sol 59
−400
Sol 63
Sol 69
Sol 74
−600
Sol 80
Sol 89
Sol 94
−800
Sol 106
Sol 166
Sol 197
−1000
Sol 235
Sol 244
Sol 257
Sol 271
Sol 285
Sol 299
−1200
Landing site
Autonomous navigation target point
Commanded navigation target point
Current site
Sol 309
Sol 323
Sol 325
−1400
0
200

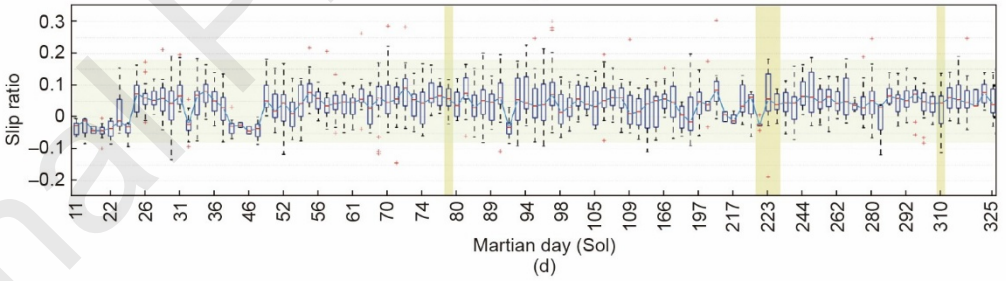
(a)


Noon
Afternoon

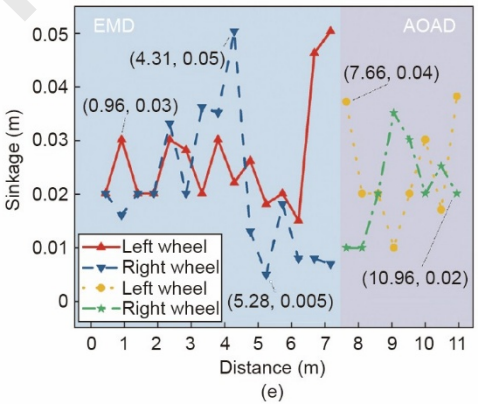
(b)


Elevation (m)
Cumulative driven distance (m)

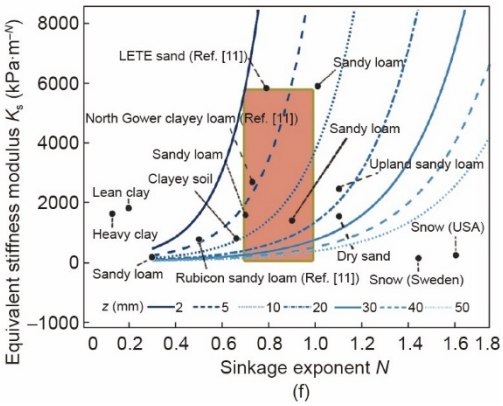
(c)


Slip ratio
Martian day (Sol)

(d)


EMD
AOAD
(4.31, 0.05)
(0.96, 0.03)
(7.66, 0.04)
(10.96, 0.02)
(5.28, 0.005)
Left wheel
Right wheel
Left wheel
Right wheel
Sinkage (m)
Distance (m)

(e)


LETE sand (Ref. [11])
Sandy loam
North Gower clayey loam (Ref. [11])
Sandy loam
Sandy loam
Upland sandy loam
Clayey soil
Lean clay
Heavy clay
Snow (USA)
Dry sand
Sandy loam
Rubicon sandy loam (Ref. [11])
Snow (Sweden)
z (mm)
Equivalent stiffness modulus K_s (kPa·m^{-N})
Sinkage exponent N

(f)

Fig. 1. Locomotion performance of the Zhurong Mars rover in wheel-rolling mode. (a) Autonomous and commanded traverse trajectories of the Zhurong Mars rover; (b) Navigation-camera views acquired at noon and in the afternoon, illustrating the illumination-driven change in the usable field of view; (c) Cumulative driven distance and corresponding elevation profile; (d) Rover slip ratio during the traverse; (e) Representative wheel sinkage variation measured on Sol 232; (f) Derived sinkage parameters updated from the measured sinkage data; terrestrial soil parameters are taken from Supplementary Table 2 of Ref. [11].

Table 1

Locomotion records from the Zhurong Mars rover at southern Utopia Planitia.

Cruise cycles	Sol	Drives (EMD + AOAD)	Sequence duration	Driven odom (m)	Locomotion tasks
1	1 | 6	1 + 0	30 min	5.5	Downslope movement
2	7 | 19	3 + 2	7 h 32 min	21	Rotation in place; circular path movement; approximately linear movement; high curvature turning
3	20 | 39	14 + 12	20 h 32 min	180	Approximately linear movements; bypassing a small impact crater

Journal Pre-proofs

Cruise cycles	Sol	Drives (EMD + AOAD)	Sequence duration	Driven odom (m)	Locomotion tasks
4	40 | 47	3 + 0	8 h 17 min	34.7	Approaching a large sand dune
5	48 | 53	5 + 4	7 h 35 min	69.4	Circumventing a sand dune; avoiding two impact craters
6	54 | 67	12 + 12	20 h 5 min	273.5	Avoiding gravel areas and impact craters; traversing between two sand dunes
7	68 | 80	11 + 11	14 h 2 min	182.7	Approximately linear and large curvilinear movements; traversing between impact craters and dunes

Journal Pre-proofs

Cruise cycles	Sol	Drives (EMD + AOAD)	Sequence duration	Driven odom (m)	Locomotion tasks
8	81 | 100	13 + 11	22 h 23 min	238	Approaching and then circumventing a sand dune, the path leads to the midpoint between two sand dunes; traversing two sand dunes and approaching another
9	101 | 112	10 + 8	13 h 21 min	163.6	Circumventing two dunes in sequence
10	113 | 115	1 + 0	59 min	13.4	Approximately linear movements
11	181 | 209	4 + 3	7 h 52 min	142.1	Continuous large-curvature maneuvering to avoid gravel zones

Journal Pre-proofs

Cruise cycles	Sol	Drives (EMD + AOAD)	Sequence duration	Driven odom (m)	Locomotion tasks
12	210 | 236	6 + 4	11 h 13 min	96.4	Circular movement
13	237 | 297	18 + 14	31 h 40 min	325.7	Approximately V-shaped broken linear movements; approaching and then circumventing a sand dune
14	298 | 359	9 + 9	16 h 29 min	175.5	Approximately stationary 90-degree and high-curvature turns; driving to the middle position between the dune and impact crater
14 cycles	359 sols	200 drives	182 h 30 min	1921.5	23 tasks

During stationary *in situ* observations, the rover remained immobile while the multispectral camera, Mars surface composition detector, magnetic-field sensor, and meteorological sensor were operated to investigate high-value terrain features. During mobile cruises, the meteorological sensor, subsurface radar, and magnetic-field sensor were operated throughout each traverse.

The vertical bar (|) separates the first and last sols of each cruise cycle.

Journal Pre-proofs

Locomotion tasks executed by the Zhurong Mars rover were planned as approximately linear drives, in-place rotations, circular traverses, high-curvature turns, and broken-line trajectories; frequent hazard-avoidance maneuvers were also recorded around dunes, impact craters, and gravel zones (Table 1). Stationary scientific observations and mobile payload measurements were interleaved during these tasks, resulting in stop–sense–move cruise cycles. The obtained *in situ* dataset is operationally representative of planetary surface operations and provides a useful basis for quantifying traversal limits.

No substantial degradation in AOAD performance was identified from the noon-to-afternoon change in the mast-mounted navigation and terrain camera (NaTeCam) field of view (Fig. 1(b)). Meanwhile, a pronounced photometric change was observed between the two views, implying a reduced perception margin under afternoon illumination. Relative to the noon scene, underexposure was observed over the terrain in the afternoon scene: mean luminance was reduced by 19.3% (median by 35.0%), and the fraction of dark pixels, defined by $Y < 60$ on a 0–255 scale, where Y denotes pixel luminance, increased from 14.9% to 56.0%. Accordingly, the effective brightness dynamic range of the ground region was reduced by 33%, and the fraction of high-contrast terrain edges was reduced by 19%, indicating that fewer distinctive features were available for VIO tracking. However, the drive logs show that these conditions remained within the nominal daytime operating range of the onboard perception-and-control loop for the analyzed *in situ* traverses.

Fig. 1(c) shows the cumulative distance driven by the Zhurong Mars rover on terrain with gradually increasing elevation. Accordingly, the slip ratio for each sol is plotted in Fig. 1(d), where the bars denote the variation range. The slip ratio s was defined as $s = (V_{\mathrm{cmd}} - V_{\mathrm{meas}})/V_{\mathrm{cmd}}$, where V_{cmd} and V_{meas} denote the commanded and VIO-measured travel velocities, respectively; negative values indicate that the measured travel speed exceeds the commanded travel speed. Modest variation was observed along the traversed terrain. The s value was mostly between -0.1 and 0.2, with a mean forward slip of 0.05 on slopes up to 5°; during sharper downslope movements (e.g., a $-5.7°$ descent on sol 312), brief negative slip was observed ($s = -0.19$) for several seconds. The wheel imprint analysis described in Ref. [32] was further used to verify the consistency of forward-slip estimates for cases with $0 \le s \le 1$, as detailed in Appendix A. Stereo imaging from the rear hazard-avoidance camera pair was used to reconstruct wheel tracks, generating wheel sinkage of 5–50 mm (mean ~ 23 mm) during each drive (Fig. 1(e)).

As a result, the soil sinkage exponent N ($\approx 0.7 - 1.0$) and equivalent sinkage stiffness K_{s} ($\approx 8.6 \times 10^2$ to 5.9×10^3 kPa $\cdot$ m^{-N}) were estimated, which are broadly consistent with previous Mars soil models (Fig. 1(f)) [11]. A nominal cruise of the Zhurong Mars rover consisted of an EMD segment followed by an AOAD segment. In some cases, AOAD was intermittently interrupted when the local landforms exceeded the wheel-rolling and steering limits. On sols 27–29, AOAD advanced through successive ~ 1 m steps across obstacle-dense ground, and the guidance system terminated each attempt at short intermediate targets (0.9 m, 0.2 m, 0.6 m), indicating that continuous wheel-rolling over large rocks could not be achieved. On sol 104, a substantial heading deviation reduced the usable near-field imagery and triggered a fallback to EMD, resulting from unreliable estimation of the required turning curvature. On sol 254, a steep, rocky patch induced excessive yaw drift, and the corrective maneuver required to recover the intended path exceeded the rover's steering capability; AOAD was then stopped, and EMD was used to continue the traverse. Consequently, the AOAD approached its operational limits owing to insufficient wheel-rolling capability over large obstacles and limited steering curvature under certain landform constraints.

To identify cruise challenges during rover traversal, the observed obstacles were systematically classified into three categories by linking the path-planning outcomes with the terrain characteristics inferred from the corresponding imagery. As shown in Fig. 2, loose soil areas, rocks, craters, ridges, troughs, and dunes were manually delineated across nine representative path-planning scenarios, and their characteristic dimensions were quantified using two annotated image reference scales: 0.7 m horizontal and 10 m longitudinal.

Journal Pre-proofs

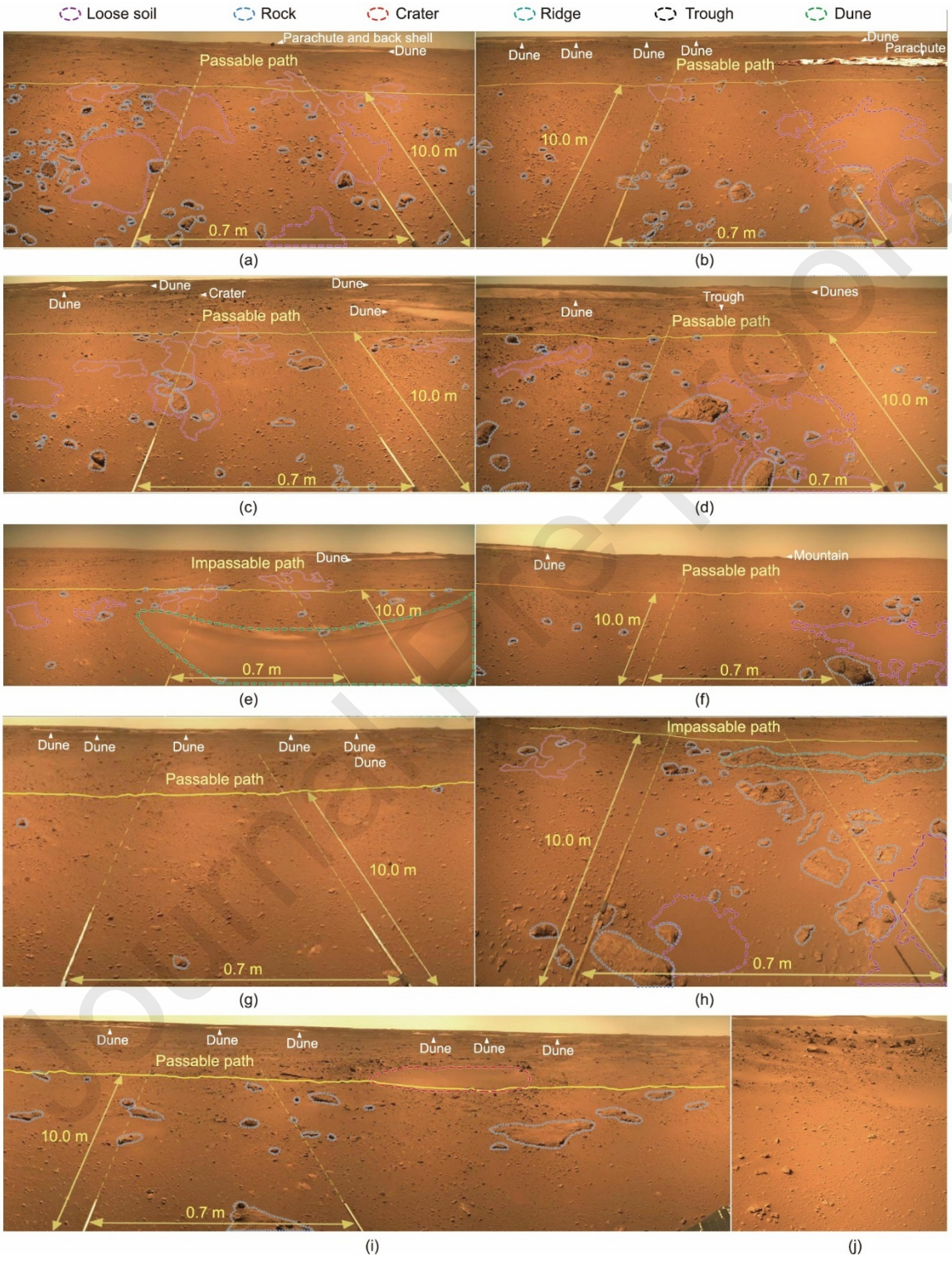

Loose soil
Rock
Crater
Ridge
Trough
Dune
Parachute and back shell
Dune
Passable path
10.0 m
0.7 m
(a)
Dune
Dune
Dune
Dune
Dune
Parachute
Passable path
10.0 m
0.7 m
(b)
Dune
Dune
Crater
Dune
Passable path
Dune
10.0 m
0.7 m
(c)
Dune
Trough
Dunes
Passable path
10.0 m
0.7 m
(d)
Impassable path
Dune
10.0 m
0.7 m
(e)
Dune
Mountain
Passable path
10.0 m
0.7 m
(f)
Dune
Dune
Dune
Dune
Dune
Dune
Passable path
10.0 m
0.7 m
(g)
Impassable path
10.0 m
0.7 m
(h)
Dune
Dune
Dune
Dune
Dune
Dune
Passable path
10.0 m
0.7 m
(i)
(j)

Fig. 2. Path-planning scenes of the Zhurong Mars rover with annotated terrain characteristics. (a) Sol 32; (b) Sol 55; (c) Sol 71; (d) Sol 86; (e) Sol 92; (f) Sol 275; (g) Sol 247; (h) Sol 255; (i) Sol 200; (j) Sol 325, showing the rover's current parking location. The horizontal yellow line marks the look-ahead distance (d=10 m) used to evaluate forward traversability. The trapezoidal region defines the forward evaluation region of interest for determining candidate paths. A candidate path is labeled as passable if the terrain features along the forward path segment satisfy a predefined passability criterion; otherwise, it is labeled as impassable.

TU is defined by broad, low-amplitude landforms that vary the wheel–terrain contact without forming discrete step-like hazards, including gentle dune bedforms, sand ridges, shallow troughs, and loose soil patches. At close range, these TU features showed rover-scale planform dimensions: ridge crests were typically 1.2–6.0 m long and 0.25–1.4 m wide; trough openings were 0.7–5.5 m wide (visible spans 2–10 m); dune bedforms showed crest-to-crest spacing of 6–18 m (single-dune spans 3–12 m); and loose-soil patches extended 0.8–4.5 m along the major axis with widths of 0.3–1.8 m. As a result, wheel-rolling mode generally remained feasible, and TU terrain was associated with a mild degradation in locomotion efficiency, characterized by modest slip-sinkage increases and limited replanning.

SOs are isolated rocks and rocky clusters that impose discrete contact constraints on individual wheels. The measured maximum rock axis ranged from 0.07 to 0.70 m (with the majority falling within 0.15–0.40 m). During the traversal of SO terrain, localized tracking disturbances (e.g., transient sinkage) were frequently induced by wheel–rock interactions, and bypass trajectories were increasingly executed by the path planner as the rock size and areal density increased.

Topographic barriers (TBs) are characterized by large, steep, or sharp-edged landforms that are difficult to safely negotiate under wheel rolling, such as crater rims/edges, steep dune faces, and pronounced terrain breaks. In the image-based measurements, rim-to-rim crater diameters ranged from 2 to 20 m, and the largest troughs and dune constructs approached the upper end of the above TU-scale ranges, forming locally steep transitions. TB-type obstacles were associated with rapid slip growth, and exceeding the onboard AOAD safety thresholds (slope 10°; obstacle height 0.12 m) resulted in autonomy termination.

In summary, a mainly mild degradation in mobility performance was observed on TU-type ground, while wheel-rolling autonomy was driven towards its reliability limits by SO and especially TB features. The observed drive interruptions were concentrated in scenes with larger and denser rocks or locally steep terrain transitions, indicating that wheel-rolling mobility degraded systematically with increasing terrain roughness, barrier-like geometry, and reduced steering curvature.

Considering the obtained obstacle geometry, travel velocity, and wheel–terrain contact forces, a set of geometric descriptors and three control indices are defined to quantify traversal difficulty as follows:

Journal Pre-proofs

(1) Geometric features are captured by the bounding rectangle (obstacle length, width, and height), obstacle clearance (area ratio within the travel zone), and obstacle-top traversability metrics, including surface flatness quantified by the plane-fitting degree M, average sharpness S_{a} of local protrusions, and longitudinal profile smoothness I_{o} along candidate wheel-contact trajectories.

(2) Trajectory-tracking smoothness μ is calculated from the magnitude of lateral and vertical accelerations. A larger μ indicates smoother tracking and reduced body vibration, with the opposite trend for smaller μ.

(3) Wheel load balance κ is inferred from the maximum differential wheel load $\Delta W_{\max}$ and the maximum deviation from the mean wheel load $\Delta W_{\mathrm{dev,max}}$ to indicate rollover risk under uneven normal-force conditions.

(4) Contact-surface complexity δ is indicated by obstacle steepness ε and roughness σ, inferred from rover attitude and wheel-force state (including lateral forces and front-rear load redistribution) to characterize the intensity of wheel–terrain interactions.

These defined quantities are calculated using a fuzzy logic inference scheme (Fig. 3). δ is obtained by fusing σ and ε after fuzzification with trapezoidal membership functions. After defuzzification, candidate obstacle-surface trajectories are ranked by grey relational analysis (GRA) using the three obstacle-top indicators ($M,\ S_{\mathrm{a}},\ I_{\mathrm{o}}$). The motion-risk level ν_1 is inferred from (δ, κ) for partial wheel suspension, while ν_2 is inferred from (δ, μ) for full wheel contact. Both levels are used for online motion-safety gating. To balance predictive adequacy and interpretability, the breakpoints of the membership functions and fuzzy rules were determined using a hybrid data-driven and expert-guided procedure. Breakpoints were initialized from distribution-based data and refined using semantic constraints, including ordering, monotonicity, and plausible thresholds. Candidate rules were weighted from the data, pruned using objective criteria, and finalized by expert review for consistency.

Journal Pre-proofs

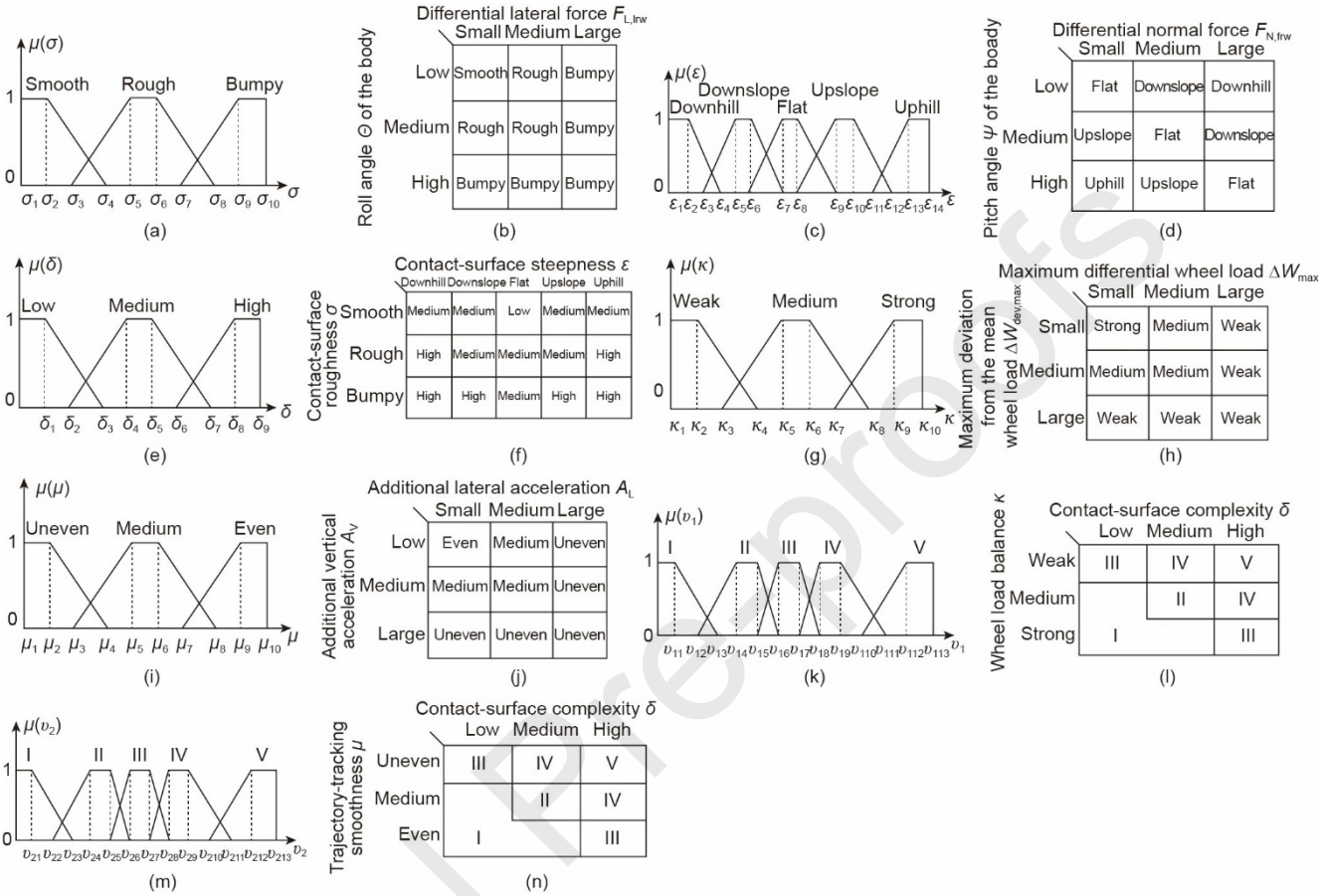


Fig. 3. Linguistic fuzzy sets and rule bases used in the designed fuzzy-logic module. (a, c) Membership functions of contact-surface roughness σ and contact-surface steepness ε; (b, d) rule tables used to infer σ from rover roll angle Θ and differential lateral force $F_{\mathrm{L,lrw}}$, and ε from rover pitch angle Ψ and differential normal force $F_{\mathrm{N,frw}}$, respectively; (e, f) membership functions of contact-surface complexity δ and the rule table mapping (σ, ε) to δ; (g, h) membership functions of wheel load balance κ and the rule table mapping the maximum differential wheel load $\Delta W_{\max}$ and the maximum deviation from the mean wheel load $\Delta W_{\mathrm{dev,max}}$ to κ; (i, j) membership functions of trajectory-tracking smoothness μ and the rule table mapping additional lateral and vertical accelerations $(A_{\mathrm{L}}, A_{\mathrm{V}})$ to μ; (k, l) membership functions and rule table for motion-risk level v_1 under partial wheel suspension above the ground, obtained from (δ, κ); (m, n) Membership functions and rule table for motion-risk level v_2 under full wheel contact with the obstacle, obtained from (δ, μ).

Journal Pre-proofs

2.2. Multimode action library and decision-making for the Zhurong-like self-reconfigurable rover

To enhance traversability beyond wheel-rolling on obstacle-dense Martian terrain, a mechanics-constrained multimode action library was constructed for Zhurong-like self-reconfigurable rovers. The library provides an explicit bridge between actuator-level capabilities and obstacle-level traversal requirements, enabling reproducible multimode execution and quantitative reasoning about mobility limits. The actuation functions are categorized into four classes according to the mechanical structure of the rover: active suspension, passive suspension, wheel driving, and wheel steering. To provide a unified representation of spatial coordination among movable joints and the associated temporal execution complexity, combinations of classes are organized into phases (defined by the number of engaged actuators) and levels (defined by the number of distinct action steps), as shown in Table 2. This library provides an effective mechanism for tracking the degree of mechanical reconfiguration during rover motion.

Table 2

Simplified motion library for the movable joints of the Zhurong-like Mars rover.

Motion action level (chronologically)	Motion action phase (spatial order)								
	Active suspension rocker class		Passive suspension rocker class		Wheel driving class		Wheel steering class	Functionality of the motion actions	
	Left active rocker-bogies rotation	Right active rocker-bogies rotation	Left passive rocker-bogies rotation	Right passive rocker-bogies rotation	Left wheel rolling	Right wheel rolling	All wheel rotation	Left side of the rover body box	Right side of the rover body box
1	-1	-1	0	0	2	2	2/1/0	Middle wheels are lifted relative to the ground	

Journal Pre-proofs

Motion action level (chronologically)	Motion action phase (spatial order)							Functionality of the motion actions	
	Active suspension rocker class		Passive suspension rocker class		Wheel driving class		Wheel steering class		
	Left active rocker-bogies rotation	Right active rocker-bogies rotation	Left passive rocker-bogies rotation	Right passive rocker-bogies rotation	Left wheel rolling	Right wheel rolling	All wheel rotation	Left side of the rover body box	Right side of the rover body box
2	-1	-1	0	1	2	2	2/1/0	Middle wheel is lifted relative to the ground	Body box is lifted relative to the ground
3	-1	-1	1	1	2	2	2/1/0	Rover chassis is lifted relative to the ground	
4	-1	0	0	0	2	1	2/1/0	Middle wheel is lifted relative to the ground	Wheel rolling while rocker-bogies stationary
5	-1	0	0	1	2	1	2/1/0	Middle wheel is lifted relative to the ground	Wheel rolling with movable rocker-bogies

Journal Pre-proofs

Motion action level (chronologically)	Motion action phase (spatial order)							Functionality of the motion actions	
	Active suspension rocker class		Passive suspension rocker class		Wheel driving class		Wheel steering class		
	Left active rocker-bogies rotation	Right active rocker-bogies rotation	Left passive rocker-bogies rotation	Right passive rocker-bogies rotation	Left wheel rolling	Right wheel rolling	All wheel rotation	Left side of the rover body box	Right side of the rover body box
6	-1	0	1	0	2	1	2/1/0	Body box is lifted relative to the ground	Wheel rolling while rocker-bogies stationary
7	-1	0	1	1	2	1	2/1/0	Body box is lifted relative to the ground	Wheel rolling with movable rocker-bogies
8	-1	1	0	0	2	2	2/1/0	Middle wheel is lifted relative to the ground	Front or rear wheel is lifted relative to the ground

Journal Pre-proofs

Motion action level (chronologically)	Motion action phase (spatial order)							Functionality of the motion actions	
	Active suspension rocker class		Passive suspension rocker class		Wheel driving class		Wheel steering class		
	Left active rocker-bogies rotation	Right active rocker-bogies rotation	Left passive rocker-bogies rotation	Right passive rocker-bogies rotation	Left wheel rolling	Right wheel rolling	All wheel rotation	Left side of the rover body box	Right side of the rover body box
9	-1	1	0	1	2	2	2/1/0	Middle wheel is lifted relative to the ground	Body box is lowered relative to the ground
10	-1	1	1	0	2	2	2/1/0	Body box is lifted relative to the ground	Front or rear wheel is lowered relative to the ground
11	-1	1	1	1	2	2	2/1/0	Body box is lifted relative to the ground	Body box is lowered relative to the ground
12	0	0	0	0	0	0	2/1/0	Wheel rotation in place	

Journal Pre-proofs

Motion action level (chronologically)	Motion action phase (spatial order)							Functionality of the motion actions	
	Active suspension rocker class		Passive suspension rocker class		Wheel driving class		Wheel steering class		
	Left active rocker-bogies rotation	Right active rocker-bogies rotation	Left passive rocker-bogies rotation	Right passive rocker-bogies rotation	Left wheel rolling	Right wheel rolling	All wheel rotation	Left side of the rover body box	Right side of the rover body box
13	0	0	0	0	1	1	2/1/0	Wheel rolling with locked rocker-bogies	
14	0	0	0	1	0	0	2/1/0	Stationary	Wheel rotation with movable rocker-bogies
15	0	0	0	1	1	1	2/1/0	Wheel rolling with locked rocker-bogies	Wheel rolling with movable rocker-bogies
16	0	0	1	1	0	0	2/1/0	Wheel rotation with movable rocker-bogies	

Journal Pre-proofs

Motion action level (chronologically)	Motion action phase (spatial order)							Functionality of the motion actions	
	Active suspension rocker class		Passive suspension rocker class		Wheel driving class		Wheel steering class		
	Left active rocker-bogies rotation	Right active rocker-bogies rotation	Left passive rocker-bogies rotation	Right passive rocker-bogies rotation	Left wheel rolling	Right wheel rolling	All wheel rotation	Left side of the rover body box	Right side of the rover body box
17	0	0	1	1	1	1	2/1/0	Wheel rolling with movable rocker-bogies	
18	0	1	0	0	1	1	2/1/0	Wheel rolling with locked rocker-bogies	Front or rear wheel is lifted relative to the ground
19	0	1	0	1	1	1	2/1/0	Wheel moving with locked rocker-bogies	Body box is lowered relative to the ground
20	0	1	1	0	1	1	2/1/0	Wheel rolling with movable rocker-bogies	Front or rear wheel is lifted relative to the ground

Journal Pre-proofs

Motion action level (chronologically)	Motion action phase (spatial order)							Functionality of the motion actions	
	Active suspension rocker class		Passive suspension rocker class		Wheel driving class		Wheel steering class		
	Left active rocker-bogies rotation	Right active rocker-bogies rotation	Left passive rocker-bogies rotation	Right passive rocker-bogies rotation	Left wheel rolling	Right wheel rolling	All wheel rotation	Left side of the rover body box	Right side of the rover body box
21	0	1	1	1	1	2	2/1/0	Wheel rolling with movable rocker-bogies	Body box is lowered relative to the ground
22	1	1	0	0	2	2	2/1/0	Front or rear wheels are lowered relative to the ground	
23	1	1	0	1	2	2	2/1/0	Front or rear wheel is lowered relative to the ground	Body box is lowered relative to the ground
24	1	1	1	1	2	2	2/1/0	Body box is lowered relative to the ground	

To reduce table length, symmetric left–right joint motions are omitted. The wheel-steering class ("All wheel rotation") is defined by three discrete steering configurations: 0 (WCM-0) for rectilinear motion, 1 (WCM-1) for curvilinear motion, and 2 (WCM-2) for crabbing motion. Accordingly, the notation 2/1/0 indicates that each motion-action level can be combined with any of the

Journal Pre-proofs

three steering configurations, with class 2 emphasized as the crabbing steering configuration, enabling lateral maneuvers. In the active-rocker rotation columns, −1 denotes a negative rotation command (opposite to +1); 0 denotes no rotation.

To ensure the feasibility of the established action library on the Zhurong Mars rover, motion constraints have been defined by limiting the action space with coordination and safety rules, under which independent steering of each wheel is permitted, suspension-driving coupling is coordinated on each body side, rocker motion is enforced symmetrically, and lifting is limited to no more than one wheel per body side. Consequently, the practical set of discrete actions was reduced to 120 (Table 2) and further grouped into six fundamental mobilities: wheel rolling mode (WRM), rover chassis lifting mode (RCLM), rover creeping mode (RCM), single-wheel lifting mode (SWLM), double-wheel lifting mode (DWLM), and wheel crabbing mode (WCM), accompanied by their derivative variants.

To differentiate the mobility performance of each mode, the modes are characterized by quantifiable metrics, including suitable terrain type, achievable speed, turning ability, energy efficiency, and recoverability from failures. Relatively smooth or gently sloping ground can be traversed in WRM for efficient travel. On soft sand or under increasing sinkage, RCM should be activated, where rocker motions redistribute the wheel loads to reduce sinkage and improve traction. For large vertical obstacles or steep scarps, RCLM or wheel lifting modes can be utilized for crossing or climbing, and small rocks can generally be overcome by SWLM. WCM should be utilized to bypass hazards or align laterally with the planned path by steering wheels around their vertical axis and then driving sideways.

Moreover, motion actions from the library are combined to realize rover reconfiguration, and an optimal action sequence is selected by mode decision-making according to the characterized terrain-traversal difficulty. Under the observed obstacle morphology and mechanics-based constraints of the rover, adaptive mode switching beyond regular wheel rolling is achieved. Specifically, the optimal motion mode is determined according to three control objectives: ① high traction to limit wheel sinkage and slip, ② OT to climb over or bypass hazards, and ③ trajectory tracking to ensure feasible local trajectory generation and path following. The corresponding mobility capabilities, including fast traversal, sinkage escape, hurdle overcoming, obstacle climbing, and obstacle avoidance, are organized within a proposed three-layer “Look, Touch, and Move” strategy, through which each terrain challenge is matched to the appropriate mode actions.

In the initial Look layer, the positional relationship between terrain obstacles and the planned trajectory and obstacle profile dimensions is evaluated. If the distribution of obstacles whose perpendicular distances to the path are within a preset threshold is too dense for safe traversal in any motion mode, replanning is triggered. Otherwise, the wheel–obstacle contact form and entrance/exit angles are analyzed. If the predicted contact poses an overturning risk, replanning is activated; otherwise, the decision proceeds to the second layer to determine a candidate motion mode. Based on the relative size of the obstacles with respect to the rover’s wheel, wheel–obstacle contact forms were classified into five types in this study: steps (e.g., small rocks), walls (e.g., large rocks), steep hybrid slopes (e.g., complex rocks), gentle slopes (e.g., craters), and pits (e.g., trenches).

In the Touch layer, the feasibility of crossing or climbing is determined after traversal towards the obstacle has been commanded. Obstacle height and upper-surface sharpness are evaluated against the motion capabilities of RCLM and wheel-lifting modes. If the obstacle is traversable with a non-contact lifting motion, an optimal mode is selected; otherwise, the contact fitness between the obstacle surface and wheel rim is further assessed. If climbing is judged as infeasible, replanning is activated; otherwise, the decision proceeds to the third layer to determine an execution mode during traversal.

In the Move layer, motion safety is evaluated in real time using three defined control indices: trajectory-tracking smoothness μ, wheel load balance κ among wheels in ground contact, and contact-surface complexity δ at the wheel–obstacle interface. These metrics are further combined to define two fuzzy logic-based motion risk indices for governing motion execution, denoted ν_1 for partial wheel suspension above the ground and ν_2 for full wheel contact with the obstacle. In both cases, a larger ν indicates higher risk (levels I–V); levels I and II correspond to very safe and safe motion, respectively. If the motion is judged safe, the current mode is maintained; otherwise, the rover is rerouted or driven in reverse to avoid the obstacle.

Safe traversability across diverse Martian landforms is enhanced by a library-based selection architecture, implemented as an MD–OT pipeline that autonomously selects an optimal motion mode in response to the characterized OT difficulty.

3. Results

3.1. Terrain-aware autonomous control framework for self-reconfigurable rovers

To close the loop between perceived terrain–obstacle characteristics, multimode mobility, and path planning, a terrain-aware autonomy control framework was developed for self-reconfigurable rovers, as shown in Fig. 4. The framework comprises three coupled modules: TP for terrain reconstruction, state estimation, and local trajectory generation; MD for planned trajectory and mode selection under quantified mobility limits; and OT for executing the selected motion action from the library using a specific rover model. Specifically, VIO is employed as the localization component of the TP module; the image frames and inertial measurements used by VIO are acquired directly from an onboard visual inertial camera mounted on the mast. The 3D kinematic model of the Zhurong Mars rover adopted in this study followed the detailed formulation reported in Refs. [33,34].

Journal Pre-proofs

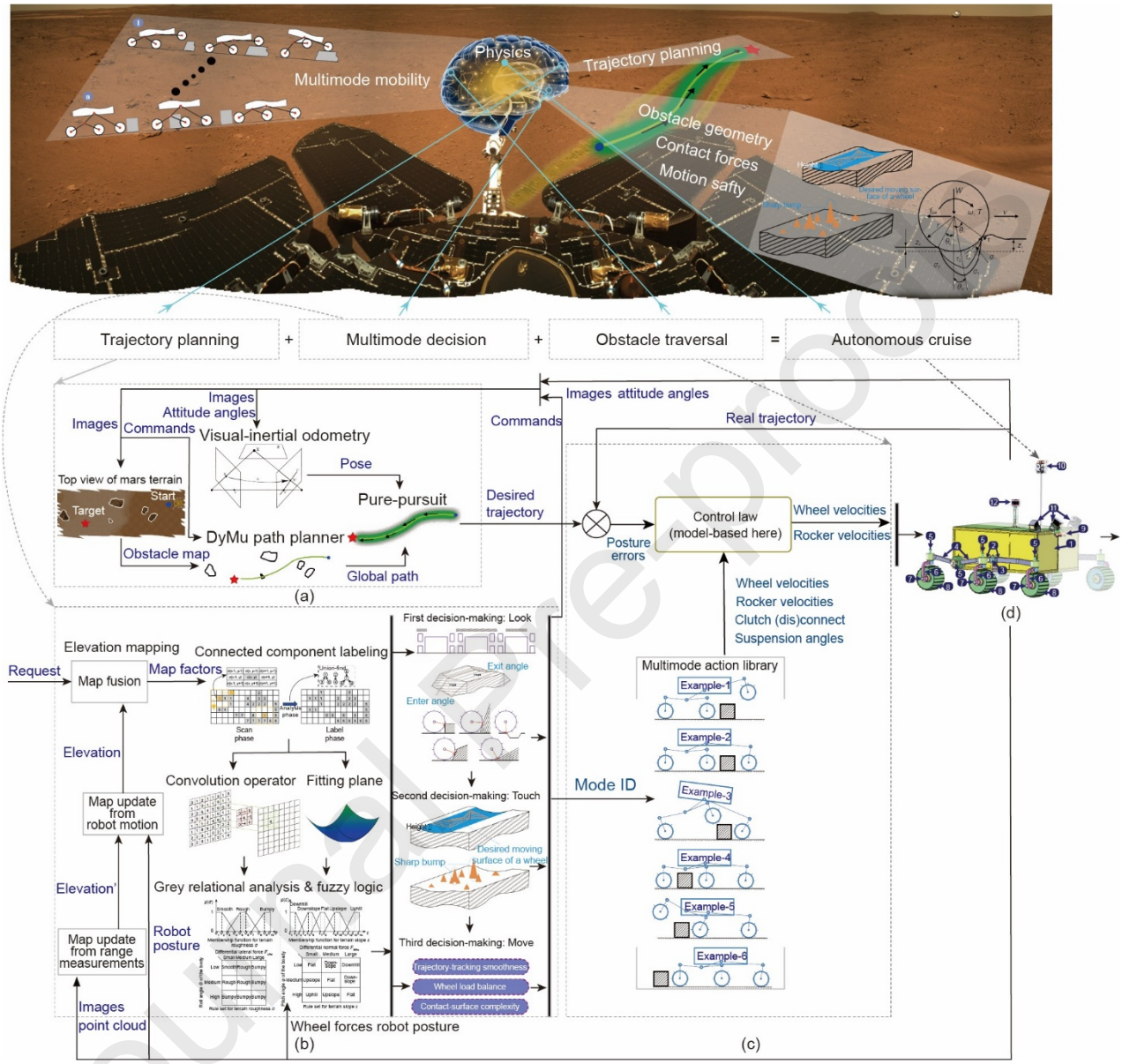


Fig. 4. Physics-informed autonomous cruise framework for the Zhurong-like self-reconfigurable rovers: (a) TP module; (b) MD module; (c) OT module; (d) Harbin Institute of Technology-Mars Rover II (HIT-MRII) rover model.

To ensure reliable autonomy control under irregular obstacle geometry and perception uncertainty, a low-compute algorithm set was employed in the TP–MD pipeline to provide reliable terrain parameterization and decision-making inputs. First, elevation mapping was used to construct a height/slope map for obstacle

detection and cost-map planning. The resulting obstacle map was then segmented into individual hazard instances using connected component labeling, enabling density checks and replanning. Next, surface feature extraction was performed to parameterize obstacle-top morphology from the elevation map for downstream decision indices. The candidate wheel-contact regions were subsequently screened using a fitting plane (FP) by evaluating the wheel-supporting planarity. GRA was then applied to rank candidate wheel-contact paths on the nonplanar obstacle upper surface using three defined indicators—plane-fitting degree, surface sharpness, and longitudinal profile smoothness—while a reject margin was enforced to flag "no-safe-path" cases.

To implement a mode-safety gate without requiring high-fidelity rover-environment interaction models, a fuzzy logic rule base was designed using the defined terrain-feature and contact-form descriptors ($\sigma,\ \varepsilon,\ \delta$) along with motion-state descriptors ($\kappa,\ \mu$). The rule base was constructed in two coupled stages. First, joint (σ,ε) conditions were mapped to δ through fuzzy logic rules, enabling consistent complexity labeling across obstacle types rather than relying on a single slope or roughness threshold. Second, two contact-state-dependent rule sets were used: (δ, κ) was mapped to ν_1 for partial wheel suspension, while (δ, μ) was mapped to ν_2 for full wheel contact. Safety margins were maintained during mode switching between lifting-related and obstacle-contact traversal modes.

3.2. Experimental validation

To evaluate the autonomous cruising performance of the Zhurong-like rover prototype Harbin Institute of Technology-Mars Rover II (HIT-MRII) (Fig. 4(d)), experiments were conducted at a Mars-analog test site. Compared with the Zhurong Mars rover, the HIT-MRII is additionally equipped with six-axis force/torque sensors integrated into each wheel axle. The experimental setup and traversal sequence are shown in Fig. 5. Four waypoints were set: the first and third (green stars) as pass-through waypoints, and the second and fourth (red stars) as stationary observation points (Fig. 5(a)). Five simulated Martian obstacle types were placed sequentially: a small ridge, large rock, trough, large mesa, and sloped loose soil bedform inclined at 15°.

The HIT-MRII rover initially cruised in WRM until encountering a small ridge (Fig. 5(k)), triggering a switch to SWLM (Fig. 5(b)) by the designed control system. It then returned to WRM (Fig. 5(c)) before reaching a large rock at the first cruise point (Fig. 5(l)). Accordingly, the rover switched to RCLM (Fig. 5(d)) and then resumed WRM (Fig. 5(e)) along the second route segment. Steering in narrow spaces was facilitated by maintaining the increased ground clearance of the lifted chassis. At the second point, the rover encountered a trough (Fig. 5(m)) and switched to WCM (Fig. 5(f)) to avoid it through a locally replanned trajectory. Upon reaching the third cruise point, the mode was switched from WCM to WRM (Fig. 5(g)). A large mesa was then encountered (Fig. 5(n)), leading to a switch to DWLM (Fig. 5(h)). The final trajectory segment was initially planned and executed in WRM (Fig. 5(i)). However, owing to insufficient traction caused by the slope and loose soil (Fig. 5(o)), the rover switched to RCM (Fig. 5(j)) to reach the destination.

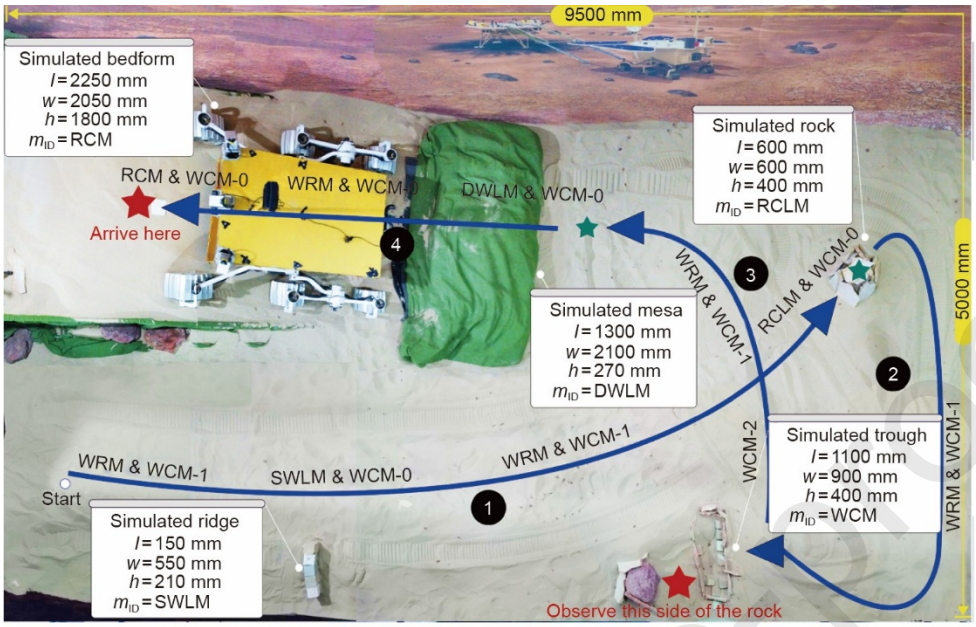
The decisions generated by the three layers of the MD module are summarized in Fig. 6. Under heterogeneous terrain conditions, the MD module acted as the decision core by reporting decision progress and safety indices associated with the selected maneuver class (Figs. 6(a) and (c), respectively). In the first layer, noncontact obstacles were assessed using geometric proximity and wheel-obstacle contact-angle

Journal Pre-proofs

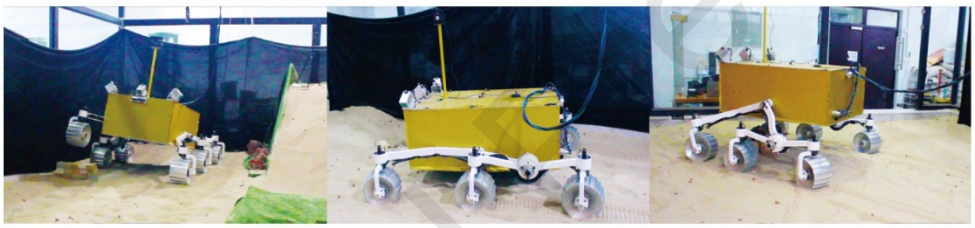
features (forward/lateral/vertical distance components and entry/exit contact angles in Fig. 6(a)). Ridge- and rock-type obstacles indicated completed mode selection and were consequently handled directly by SWLM/RCLM without activating contact-risk evaluation.

Obstacles requiring surface contact were processed in the second layer, where obstacle-top traversability was evaluated using the number of candidate paths N_{t}, plane-fitting degree M, average upper-surface sharpness S_{a}, longitudinal profile smoothness I_{o}, and GRA-based obstacle-top traversability score $\Gamma(0,i)$ (Fig. 6(b)). Here, i indexes a candidate wheel-contact trajectory, and 0 denotes the ideal reference sequence (1, 1, 1) for the three normalized indicators. The trough case showed relatively high upper-surface sharpness, and WCM was selected to bypass the hazard through local replanning. For mesa-type obstacles, favorable values of M,I_{o},N_{t}, and $\Gamma(0,i)$ were obtained, and DWLM was consequently selected for controlled climbing. In bedform and sandy-slope cases, admissible paths were retained.

Journal Pre-proofs



(a)



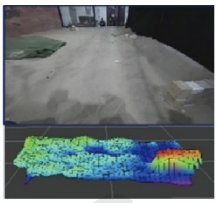
(b) (c) (d)



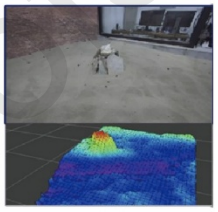
(e) (f) (g)



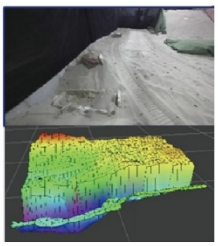
(h) (i) (j)



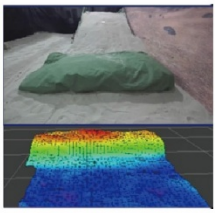
(k)



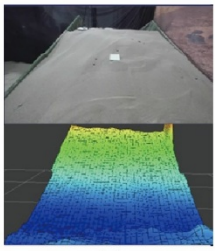
(l)



(m)



(n)



(o)

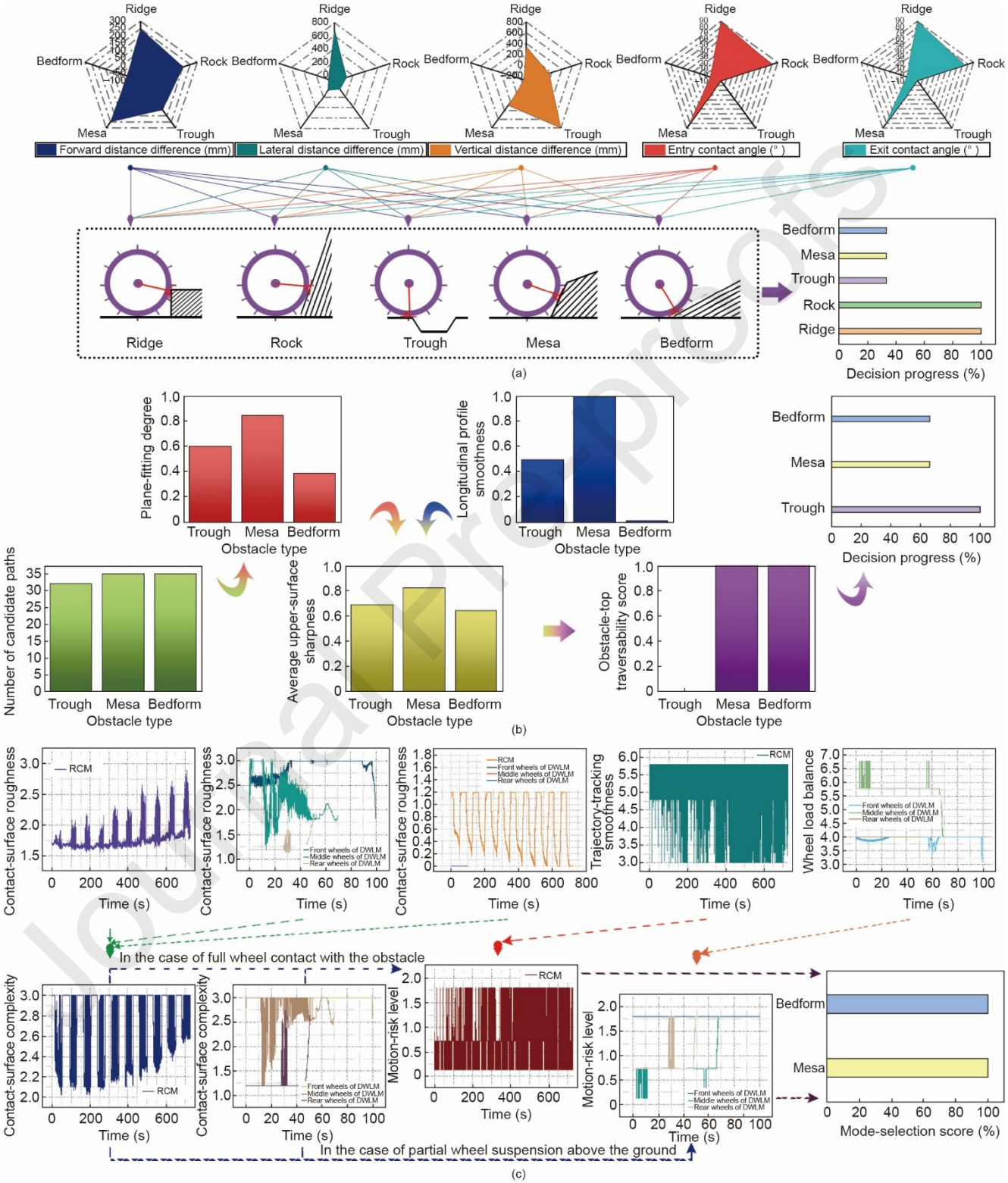
Journal Pre-proofs

Fig. 5. Experimental validation in representative Martian terrain scenarios: (a) traversed trajectory; (b) SWLM traversal; (c, e, g, i) WRM traversal shown at four stages; (d) RCLM traversal; (f) WCM traversal; (h) DWLM traversal; (j) RCM traversal; (k) simulated Martian ridge; (l) simulated Martian rock; (m) simulated Martian trough; (n) simulated Martian mesa; (o) simulated bedform. The experimental sequence is provided in Appendix A.

However, stronger indicators associated with contact angle and upper-surface sharpness were observed, and RCM was selected to improve traction. Safety during DWLM/RCM execution was governed by the third layer by evaluating the contact-surface complexity from the calculated roughness and steepness, in addition to motion smoothness and wheel load balance indices (Fig. 6(c)). Across representative climbs, the contact-surface complexity index δ remained within the low-to-intermediate range. During DWLM, ν_1 was 1.8 for front-wheel lifting and predominantly 0.72 for middle- and rear-wheel lifting, with brief increases up to 1.8. During RCM, ν_2 ranged from 0.12 to 1.8. These values remained within the safe range represented by fuzzy risk levels I and II.

Stable closed-loop performance of the developed control framework was demonstrated during a simulated 21 m cruise mission, with successful multimode decision-making and autonomous mode switching across five representative obstacle types. All target waypoints were autonomously reached in sequence, during which nine mode transitions were executed and only one local replanning operation was triggered at the trough. Moreover, across numerous independent runs under two terrain setups, the overall success rate was approximately 95%. The primary failure was attributed to perception degradation: VIO tracking was lost during high-contrast lighting transitions, and camera pose drift accumulated during mechanism reconfiguration, ultimately leading to trial termination.

Journal Pre-proofs


Ridge
Rock
Trough
Mesa
Bedform
Forward distance difference (mm)
Lateral distance difference (mm)
Vertical distance difference (mm)
Entry contact angle (°)
Exit contact angle (°)
Decision progress (%)
(a)
Plane-fitting degree
Longitudinal profile smoothness
Obstacle type
Number of candidate paths
Average upper-surface sharpness
Obstacle-top traversability score
(b)
Contact-surface roughness
Trajectory-tracking smoothness
Wheel load balance
RCM
Front wheels of DWLM
Middle wheels of DWLM
Rear wheels of DWLM
Time (s)
In the case of full wheel contact with the obstacle
Contact-surface complexity
Motion-risk level
Mode-selection score (%)
In the case of partial wheel suspension above the ground
(c)

Journal Pre-proofs

Fig. 6. Motion-mode decisions of the MD module during the autonomous cruise experiment. (a) First-layer decision for noncontact obstacles, based on the forward/lateral/vertical distance components between the HIT-MRII rover and obstacles, entry contact angle, exit contact angle, and the resulting decision progress; (b) Second-layer decision for wheel-contacting obstacles, based on the number of candidate paths, plane-fitting degree, average upper-surface sharpness, longitudinal profile smoothness, obstacle-top traversability score, and the resulting decision progress; (c) Third-layer decision for climbing maneuvers, based on contact-surface roughness, contact-surface steepness, trajectory-tracking smoothness, contact-surface complexity, wheel load balance, and the motion-risk levels, and used for mode selection. **The terrain, motion-state, and motion-risk indices are dimensionless.** Decision progress is approximately 33% and 66% after the first and second layers, respectively, while mode selection remains unresolved, and reaches 100% once a mode is determined.

3.3. Limitations and possible improvements

Among the experimental trials, failures were mainly observed during joint-action switching on uneven terrain, particularly during wheel-lifting transitions involving rapid changes in wheel loads. Under complex wheel–terrain interactions (increasing δ), the normal loads on the grounded wheels were dynamically redistributed (decreasing κ), causing slippage of the unactuated wheels and significant body-box vibration, which in certain cases manifested as μ fluctuations. In such trials, larger fluctuations coincided with degraded visual perception, characterized by fewer trackable features and geometric inliers and increased reprojection residuals.

To minimize wheel slippage, future work should explore real-time load balancing through active adjustment of the rover's center-of-mass position. To reduce high-frequency vibration transmission, the camera support and body box should be connected using appropriate damping and isolation. A systematic evaluation framework can be formulated by correlating μ,κ, and δ with selected TP metrics and by modeling failure probability via logistic regression. This provides quantitative guidance for improving posture stability during mechanical self-reconfiguration. Moreover, TP performance is constrained by the VIO-based localization component. Localization robustness could be improved through Kalman-filter-based fusion of visual, inertial, and wheel odometry measurements.

4. Discussion and conclusion

This study analyzed the synchronized drive logs of the Zhurong Mars rover and near-field imagery acquired during its *in situ* traverse in southern Utopia Planitia to derive terrain-conditioned mobility limits and to inform a terrain-aware autonomy framework for self-reconfigurable rovers. Across 200 drives, the employed autonomous wheel-rolling mode approximately doubled the mean distance per drive (13.9 m vs 6.1 m), indicating improved traverse efficiency. The *in situ* dataset was also utilized to characterize wheel–terrain interaction under Martian regolith conditions by inverting a quasi-static wheel–soil interaction model, which generated an updated sinkage exponent of $N \approx 0.7$–1.0, and to parameterize autonomy interruption conditions as measurable thresholds in steering curvature and obstacle scale.

The designed MD-OT pipeline provides a structured mechanism for mapping perceived obstacle morphology to an executable motion mode. Terrain-traversal difficulties are classified into three categories (TUs, SOs, and TBs), and the corresponding geometric descriptors (including contour size, upper-surface sharpness, and longitudinal profile) are defined for multimodal decision-making. To enable mode switching when wheel-rolling autonomy is assessed to be low-confidence or unsafe, a mechanics-constrained action library that spans wheel rolling, wheel lifting, wheel crabbing, chassis length-and-height adjustment, and body creeping was constructed. The mapping between traversal difficulty and multimode mobility is realized by the proposed three-layer "Look, Touch, and Move" control strategy, in which hazards are predicted at a standoff distance, traversability is refined after approach, and action safety is enforced online using a set of fuzzy logic-defined control indices (including contact-surface complexity, trajectory-tracking smoothness, and wheel load balance). The designed fuzzy logic algorithm effectively handles uncertainty by transforming noisy wheel-force and body-pose estimates into control indices through linguistic rules and membership functions, enabling robust decision-making.

The closed-loop feasibility of the developed autonomy control framework was demonstrated in Mars-analog cruising experiments over a 21 m route using a Zhurong-like rover prototype. In the experiments, all waypoints were reached in sequence, nine mode transitions were executed, and only one replanning event was triggered at the trough. Moreover, across independent runs under two terrain setups, the overall success rate was approximately 95%. The primary failure during mode switching was VIO tracking loss under high-contrast lighting transitions, compounded by accumulated pose drift, suggesting that perception robustness is a key limiting factor for long-range autonomy during mechanism reconfiguration on natural terrain. The obtained results provide practical guidance for advancing self-reconfigurable rover autonomy beyond wheel-rolling cruise by combining empirically grounded mobility limits with structured multimode action selection. Future work will improve perception robustness under sudden body vibrations, refine risk-gated mode selection via uncertainty-aware safety constraints, and expand field validation across broader soil states and lighting conditions.

CRediT authorship contribution statement

Huanan Qi: Conceptualization, Methodology, Software, Validation, Formal analysis, Investigation, Data curation, Visualization, Writing – original draft, Writing – review & editing. Liang Ding: Project administration, and Writing – review & editing. Ximing He: Project administration, Resources, Writing – original draft, Writing – review & editing. Haibo Gao and Zongquan Deng: Resources, Writing – review & editing. Miao Zheng, Xinyu Li, Xinyan Guo, Wenhao Feng, Lisijin Tang, and Sen Liu: Investigation. Tianyi Yu, Chuankai Liu, Baofeng Yuan, Xiaohui Liu, Zuoyu Zhang, Ruyi Zhou, Huaiguang Yang, Jing Sun, Houman Yu, Yafang Liu, Yuncheng Lin, Shaojin Han, Qian Xu, Lichun Li, Hao Lu, and Ping Jiang: Resources, Writing – review & editing. Pierangelo Masarati and Zdravko Terze: Writing – review & editing.

Declaration of competing interest

The authors declare that they have no known competing financial interests or personal relationships that could have appeared to influence the work reported in this article.

Journal Pre-proofs

Data availability

The raw data used to generate the figures in this paper are available from the corresponding author upon reasonable request. The functional structure of the multimode decision block is provided in the GitHub repository, while its specific implementation is influenced by differences in programming environments and hardware configurations.

GitHub Repository: Robot-Starscream https://github.com/Robot-Starscream/MultimodeAutonomousCruise_Rover

An experimental movie has been uploaded to the MobRoboTrans YouTube channel: https://www.youtube.com/@MobRoboTrans

Acknowledgments

This work was supported by the National Natural Science Foundation of China (52425502 and 523B2039), the National Key Research and Development Program of China (2022YFB4702300 and 2024YFB4710900), the Fundamental Research Funds for the Central University (HIT.DZJJ.2025021 and HIT.OCEF.2023042), the Self-Planned Task of State Key Laboratory of Robotics and Systems (HIT; SKLRS202503C), and the National Natural Science Foundation of China under the Basic Science Center Program for Space Robot Intelligent Manipulation (T2388101).

References

[1] Chien SA, Visentin G, Basich C. Exploring beyond Earth using space robotics. Sci Robot 2024;9(91):eadi6424.

[2] Swan RM, Atha D, Leopold HA, Gildner M, Oij S, Chiu C, et al. AI4MARS: a dataset for terrain-aware autonomous driving on Mars. In: Proceedings of the IEEE/CVF Conference on Computer Vision and Pattern Recognition Workshops; 2021 Jun 19–25; held virtually. New York City: IEEE; 2021. p. 1982–91.

[3] Rankin A, Maimone M, Biesiadecki J, Patel N, Levine D, Toupet O. Mars Curiosity rover mobility trends during the first 7 years. J Field Robot 2021;38(5):759–800.

[4] Maimone MW, Johnson AE, Cheng Y, Willson RG, Matthies LH. Autonomous navigation results from the Mars Exploration Rover (MER) mission. In: Experimental robotics IX; vol 21. Berlin, Heidelberg: Springer; 2006. p. 3–13.

[5] Biesiadecki JJ, Leger C, Maimone MW. Tradeoffs between directed and autonomous driving on the Mars Exploration rovers. Int J Robot Res 2007;26(1):91–104.

[6] Maimone MW, Cheng Y, Matthies LH. Two years of visual odometry on the Mars Exploration rovers. J Field Robot 2007;24(3):169–86.

Journal Pre-proofs

[7] Grotzinger JP, Crisp J, Vasavada AR, Anderson RC, Baker CJ, Barry R, et al. Mars Science Laboratory mission and science investigation. Space Sci Rev 2012;170(1–4):5–56.

[8] Toupet O, Biesiadecki JJ, Rankin AL, Steffy A, Meirion-Griffith G, Levine D, et al. Terrain-adaptive wheel speed control on the Curiosity Mars rover: algorithm and flight results. J Field Robot 2020;37(5):699–728.

[9] McHenry M, Abcouwer N, Biesiadecki J, Chang J, Del Sesto T, Johnson A, et al. Mars 2020 autonomous rover navigation. In: Advances in the astronautical sciences, vol 172. San Diego: Univelt; 2020. Paper No. AAS 20-101.

[10] Verma V, Maimone MW, Gaines DM, Francis R, Estlin TA, Kuhn SR, et al. Autonomous robotics is driving Perseverance rover's progress on Mars. Sci Robot 2023;8(80):eadi3099.

[11] Ding L, Zhou R, Yu T, Gao H, Yang H, Li J, et al. Surface characteristics of the Zhurong Mars rover traverse at Utopia Planitia. Nat Geosci 2022;15(3):171–6.

[12] Hedrick G, Ohi N, Gu Y. Terrain-aware path planning and map update for Mars sample return mission. IEEE Robot Autom Lett 2020;5(4):5181–8.

[13] Li Y, Chen K, Wang Y, Zhang W, Wang J, Chen H, et al. Real-time multilevel terrain-aware path planning for ground mobile robots. IEEE Trans Robot 2025;41:4159–79.

[14] Bouton A, Gao Y. MARCEL: mobile active rover chassis for enhanced locomotion. J Field Robot 2023;40(6):1504–24.

[15] Lyu S, Zhang W, Yao C, Zhu Z, Jia Z. Modeling and analysis of a reconfigurable rover for improved traversing over soft sloped terrains. Biomimetics 2023;8(1):131.

[16] Wang Y, Wan W, Gou S, Peng M, Liu Z, Di K, et al. Vision-based decision support for rover path planning. Remote Sens 2020;12(4):624.

[17] Karachevtseva IP, Kozlova NA, Kokhanov AA, Zubarev AE, Nadezhdina IE, Patratiy VD, et al. Cartography of the Luna-21 landing site and Lunokhod-2 traverse area based on lunar reconnaissance orbiter camera images and surface archive TV-panoramas. Icarus 2017;283:104–21.

[18] Gaines D, Chien S, Rabideau G, Kuhn S, Wong V, Yelamanchili A, et al. Onboard planning for the Mars 2020 Perseverance rover. In: Proceedings of the 16th Symposium on Advanced Space Technologies in Robotics and Automation; 2022 Jun 1–2; Noordwijk, the Netherlands. Paris: European Space Agency (ESA); 2022.

[19] Acosta-Amaya GA, Miranda-Montoya DA, Jimenez-Builes JA. Lightweight two-layer control architecture for human-following robot. Sensors 2024;24(23):7796.

Journal Pre-proofs

Journal Pre-proofs

[20] Cheng Y, Maimone MW, Matthies L. Visual odometry on the Mars Exploration rovers: a tool to ensure accurate driving and science imaging. IEEE Robot Autom Mag 2006;13(2):54–62.

[21] Scaramuzza D, Fraundorfer F. Visual odometry. IEEE Robot Autom Mag 2011;18(4):80–92.

[22] Elfes A. Using occupancy grids for mobile robot perception and navigation. Computer 1989;22(6):46–57.

[23] Goldberg SB, Maimone MW, Matthies L. Stereo vision and rover navigation software for planetary exploration. In: Proceedings of the IEEE Aerospace Conference; 2002 Mar 9–16; Big Sky, MT, USA. New York City: IEEE; 2002. p. 2025–36.

[24] Pairet È, Hernández JD, Carreras M, Petillot Y, Lahijanian M. Online mapping and motion planning under uncertainty for safe navigation in unknown environments. IEEE Trans Autom Sci Eng 2022;19(4):3356–78.

[25] Trautman L, Montgomery J, Alibay F, Vanelli T, Estlin T, Zarifian A. Automating surface attitude positioning and pointing operations for Mars 2020. In: Proceedings of the 2022 IEEE Aerospace Conference; 2022 Mar 5–12; Big Sky, MT, USA. New York City: IEEE; 2022. p. 1–9.

[26] Zarei M, Chhabra R. Advancements in autonomous mobility of planetary wheeled mobile robots: a review. Front Space Technol 2022;3:1080291.

[27] Wu B, Dong J, Wang Y, Rao W, Sun Z, Li Z, et al. Landing site selection and characterization of the Zhurong rover. J Geophys Res Planets 2022;127(4):e2021JE007137.

[28] Liu J, Li C, Zhang R, Rao W, Cui X, Geng Y, et al. Geomorphic contexts and science focus of the Zhurong landing site on Mars. Nat Astron 2022;6(1):65–71.

[29] Chen Z, Wu B, Wang Y, Liu S, Li Z, Yang C, et al. Rock abundance and erosion rate at the Zhurong landing site in southern Utopia Planitia. Earth Space Sci 2022;9(8):e2022EA002252.

[30] Xiao L, Huang J, Kusky T, Head JW, Zhao J, Wang J, et al. Evidence for marine sedimentary rocks in Utopia Planitia. Natl Sci Rev 2023;10(9):nwad137.

[31] Li J, Liu H, Meng X, Duan D, Lu H, Zhang J, et al. Ancient ocean coastal deposits imaged on Mars. Proc Natl Acad Sci U S A 2025;122(9):e2422213122.

[32] Li N, Gao H, Ding L, Lv F, Bi Z, Wang Y. Research on feature extraction and segmentation of rover wheel imprint. J Supercomput 2020;76(4):2357–73.

[33] Ding L, Qi H, Li X, Li S, Cheng Q, Yang H, et al. 3D kinematic modeling of a self-reconfigurable wheeled mobile robot for enhancing multimode motion capability. Int J Robot Res 2026. https://doi.org/10.1177/02783649261458409.

Journal Pre-proofs

[34] Qi H, Li X, Ding L, Cheng Q, Gao H, Terze Z, et al. Enhancing maneuverability in a variable wheelbase wheeled mobile robot through dynamic steering curvature control. J Field Robot 2025;42(4):1244–70.

[35] Qi H, Ding L, Zheng M, Huang L, Gao H, Liu G, et al. Variable wheelbase control of wheeled mobile robots with worm-inspired creeping gait strategy. IEEE Trans Robot 2024;40:3271–89.

[36] Qi H, Ding L, Yang H, Guo X, Li S, Gao H, et al. Autonomous creeping mode control for traction enhancement and energy optimization in self-reconfigurable wheeled mobile robots. IEEE Trans Syst Man Cybern Syst 2025;55(10):6530–44.

Declaration of Interest Statement

The authors declare that they have no known competing financial interests or personal relationships that could have appeared to influence the work reported in this paper.

If any competing interests exist, they should be disclosed here in accordance with the journal's policy.

Journal Pre-proofs